

Analysis and classification of broadband echoes using bio-inspired dolphin pulses

Yan Pailhas,^{a)} Chris Capus, and Keith Brown

Oceans Systems Laboratory, School of EPS, Heriot-Watt University, Edinburgh, Scotland EH14 4AS, United Kingdom

Patrick Moore

SPAWAR Systems Center San Diego, 53560 Hull Street, San Diego, California 92152

(Received 28 April 2009; revised 4 March 2010; accepted 5 March 2010)

To date most sonars use narrow band pulses and often only the echo envelope is used for object detection and classification. This paper considers the advantages afforded by bio-inspired sonar for object identification and classification through the analysis and the understanding of the broadband echo structure. Using the biomimetic dolphin based sonar system in conjunction with bio-inspired pulses developed from observations of bottlenose dolphins performing object identification tasks, results are presented from experiments carried out in a wave tank and harbor. In these experiments responses of various targets to two different bio-inspired signals are measured and analyzed. The differences in response demonstrate the strong dependency between signal design and echo interpretation. In the simulations and empirical data, the resonance phenomena of these targets cause strong notches and peaks in the echo spectra. With precision in the localization of these peaks and dips of around 1 kHz, the locations are very stable for broadside insonification of the targets and they can be used as features for classification. This leads to the proposal of a broadband classifier which operates by extracting the notch positions in the target echo spectra.

© 2010 Acoustical Society of America. [DOI: 10.1121/1.3372754]

PACS number(s): 43.80.Ka, 43.60.Bf [MCH]

Pages: 3809–3820

I. INTRODUCTION

In recent years improvements in the quality of sidescan sonar imagery accompanied by major advances in image-based classification techniques have led to considerably better performance in automated target detection and identification.^{1–6} Correct classification rates in excess of 90% can be achieved using advanced techniques such as multi-classifier fusion.^{7–10} To improve further on these results, the main research focus is shifting toward ever higher resolution systems, such as synthetic aperture sonar, requiring more complex hardware and platforms. Broadband sonar offers an alternative low-cost route to classification with the potential to exceed the performance of current sidescan and forward-look solutions through consideration of target responses over a wide range of frequencies.

The natural resonances of targets influence the broadband echo and have been identified as valuable candidates for classification purposes.¹¹ Significant research on broadband classification is found in the fisheries domain for the identification of species from acoustic backscatter responses.^{12–14} In this paper we are interested in the application of broadband sonar to the classification of fabricated targets and in relating echo responses to physical properties of the targets.

The excellent acoustic target detection and identification capabilities of the bottlenose dolphin (*Tursiops truncatus*)

are well documented.¹⁵ Dolphins consistently outperform fabricated systems, especially in complex acoustic environments such as shallow water or over cluttered seabeds. Working in these difficult environments the clicks and patterns of interpretation used must be robust to noise and reverberation noise in particular. Compared to conventional narrowband sonar, wideband dolphinlike signals are expected to provide some improvement through pulse compression, and for certain difficult maritime targets have been shown to provide improved detection ranges.^{11,16} Recognition is a more complex task, and research has shown that dolphins can learn to distinguish objects' shapes, materials, and contents acoustically.¹⁷ Even though the interpretation and identification requires complex analysis, this shows that the information hidden in the return signal contains target parameters that are useful for classification purposes.

In Sec. II we introduce necessary background on the physics of acoustic scattering for cylindrical shells. Analytic solutions for broadband pulses are provided and differences between models for the echo structure for low impedance and high impedance materials are discussed. To mitigate computation demands, an important step in our calculations is the specification of a truncated sum for the form function f_∞ . The form function f_∞ represents the frequency response of the target in the far field. A full justification for this approximation is given in an appendix.

For more complex targets the theoretical analysis becomes intractable. Section III shows that a numerical approach using a finite difference time domain (FDTD) simu-

^{a)}Author to whom correspondence should be addressed. Electronic mail: Y.Pailhas@hw.ac.uk

TABLE I. Parameters used to compute the theoretical form functions of three cylindrical shells: a PVC tube, a steel pipe, and a thin walled aluminum flask (aluminum bottle). Note that all acoustical parameters can be found in Ref. 21.

Material	Outer diameter a (m)	Inner diameter b (m)	Mass density ρ (kg m ⁻³)	Compressional velocity c_l (m s ⁻¹)	Shear velocity c_s (m s ⁻¹)
PVC tube	0.170	0.164	1380	2380	1200
Steel pipe	0.168	0.142	7900	5900	3200
Aluminum bottle	0.0814	0.0798	2700	6420	3040

lator can provide a good alternative solution to analytic computation, with excellent agreement between theoretical and numerical models.

Section IV introduces empirical data gathered using the biomimetic dolphin based sonar (DBS) system. We investigate the impact on the echo structure of different bio-inspired pulses and compare analytic solutions, numerical models, and experimental results from the Heriot-Watt University test tank and a working harbor environment.

In Sec. V a novel classifier is proposed based on features of the echo spectra, which are dependent on the inner resonances of the objects under broadside insonification. Experimental results are presented for five different targets. We show that even with pulses covering the same nominal bandwidth, there are strong variations in performance, with some producing better results than others in terms of discrimination potential. The generally high performance of this simple classifier supports the hypothesis that object resonances do offer good features for classification.

II. THEORETICAL BACKGROUND

To aid understanding of the processes of echo formation in different sorts of targets, this section provides a brief discussion of the physics underlying acoustic backscattering from cylindrical shells, paying particular attention to the influence of different materials. In relation to broadband classification, the aim is to link interferences in the echo spectra to the shape and material properties of the insonified targets.

A. Calculation of the form function

An analytic solution for the pressure field scattered by simple shaped objects can be computed using a decomposition in modes. The case of the elastic cylindrical shell involves solving the system of equations by Cramer's rules, with the exact solution for an infinite cylindrical shell proposed by Doolittle.¹⁸ This resolution comes from a modal decomposition, and in the case of far field backscatter we derive

$$p_s = P_0 \sqrt{\frac{2}{\pi kr}} e^{jkr} e^{-j\pi/4} f_\infty e^{j\omega t}. \quad (1)$$

Note that r represents the distance from the center of the cylinder to the receiver and k is the wavenumber. The form function f_∞ is given by $\sum_{n=0}^{\infty} (-1)^n \epsilon_n b_n$, where b_n is the solution of a system of equations and is determined by the ratio of two 6×6 determinants as suggested by Cramer. b_n is a function of the density and the compressional velocity of the two fluids inside and outside the cylinder, the dimensions a

and b (outer and inner diameters, respectively), the density, and the acoustic properties (c_l and c_s) of the cylinder material. As a result the form function f_∞ is a function of the frequency, the dimensions of the cylinder, and its acoustic properties. To be more precise, the form function has the dependencies $f_\infty(ka, k_L, k_T, a, b)$, where $k = 2\pi f / c_{\text{water}}$, $k_L = 2\pi f / c_l$, and $k_T = 2\pi f / c_s$. So for a given cylinder where dimensions and material are fixed, f_∞ is reduced to a function of the frequency alone. It is this dependency we will study in Secs. III–V.

In our computation f_∞ is approximated by the truncated sum $\sum_{n=0}^N (-1)^n \epsilon_n b_n$ with $ka < N/2$. A justification of this approximation is given in the Appendix.

These results are defined for an incoming plane monochromatic sound wave. However an extension for any incoming pulse $g_i(t)$ was proposed by Hickling.¹⁹ This is a linear system resulting in the frequency representation of the echo $g_s(\omega)$ given in Eq. (2)

$$g_s(\omega) = \frac{a}{2r} f_\infty \int_{-\infty}^{+\infty} g_i(\tau) e^{jka\tau} d\tau, \quad (2)$$

with $\tau = (ct - r/a)$. The theoretical echo in the time domain results from inverting this expression through the inverse Fourier transform.

B. Theoretical predictions

We use the theoretical results from Sec. II A to calculate predicted echoes for two cylinders: a PVC tube and a steel pipe. The cylinder parameters are taken from two real targets we have used extensively in experiments with the DBS (see Sec. IV B). Stanton has proposed some approximations derived from the ideal case to extend the formulae to finite and deformed cylinders.²⁰ For the current case, finite straight cylinders, only a multiplicative factor depending on the length is required. The form function f_∞ does not change as long as the angle of incidence stays close to normal.

Required parameters for the two cylinders and for a thin walled aluminum bottle used in some of the later experiments can be found in Table I. Figure 1 displays the form functions $|f_\infty|$ for the cylinders. We estimate from empirical data that the peak target strength of the steel pipe is approximately 1.6 dB above the target strength of the polyvinyl chloride (PVC) tube. The theoretical computation gives a difference of $2 \text{ dB} \pm 1 \text{ dB}$ in the range of 90–110 kHz, validating the measurement. An important point here is that at high frequencies (80–130 kHz), the peak values of $|f_\infty|$ for

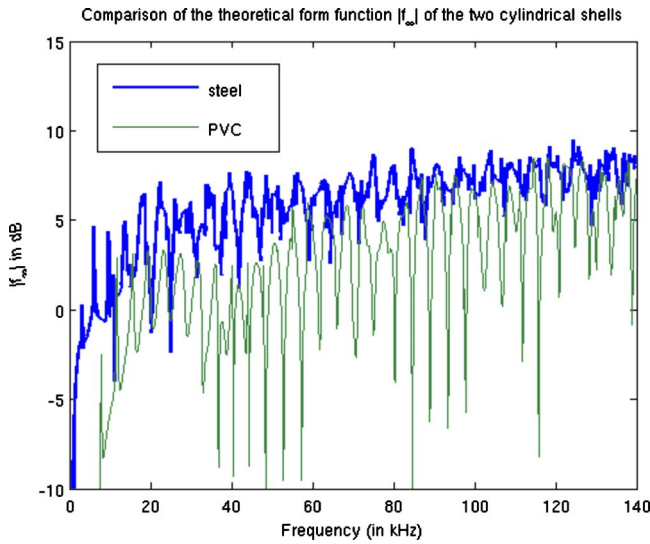


FIG. 1. (Color online) Theoretical form functions $|f_\infty|$ for the PVC tube and the steel pipe.

both materials are very similar. Conversely, at lower frequencies (30–80 kHz), the peaks are separated by a mean of 4.5 dB.

C. Echo structure modeling

The background acoustics theory presented in Sec. II A provides the basis for our target echo comparisons. For conventional narrowband sonar we would wish to avoid regions of the spectrum with strong oscillations in the form function since these could adversely affect detection of some objects. In the wideband case the oscillations will form the basis for classification and we target higher ka -values. Considering a bandwidth from 60 to 130 kHz, with principal target dimensions of typically 10–20 cm, the investigation covers frequencies defined by the range ka from 10 to 50, where k is the wavenumber associated with wavelength λ and a is a key target dimension, e.g., radius for a cylinder. For these targets and frequency range, the resonance scattering theory predicts the presence of strong peaks and notches in the echo spectra.^{22–24}

The notches arise from interferences due to the integration in time of the different echoes. The first major contribution comes from the direct reflection and is called the specular echo. We are interested here in the time delay between the specular echo and large secondary echoes, since these time delays will determine the principal notch spacings.

1. Echo structure for cylindrical shell with low impedance material

Under the assumption that the first two major contributions to the echo are primarily due to reflections from the front and back walls of the PVC cylinder, the expected time spacing is approximated by

$$\tau = 2 \left(\frac{\delta}{c_{\text{cyl}}} + \frac{b}{c} \right), \quad (3)$$

where δ is the thickness of the wall, c_{cyl} the sound speed in the cylinder material, and b is the inner diameter.

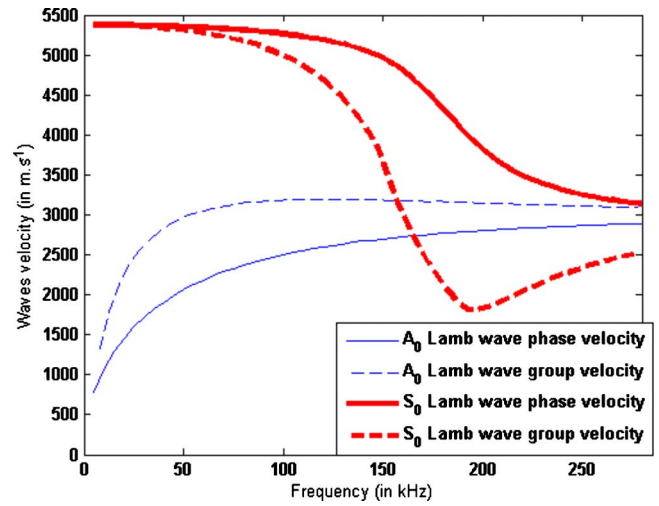


FIG. 2. (Color online) Dispersion plot of the phase and group velocities associated to the first Lamb waves A_0 and S_0 in a steel plate with 13 mm thickness.

This assumption is built on the observation that the tube wall is thin ($b/a \approx 0.96$), and the water/PVC impedance mismatch is small in comparison with metal. This allows acoustic transmission into the interior of the cylinder and the timing between the main echoes is expected to give a good approximation to the internal diameter ($b \approx \pi c/2$). Numerical simulation sheds more light on the processes of echo formation and allows us to develop a more accurate approximation based on an analogy with geometrical optics (see Sec. III B).

2. Echo structure for cylindrical shell with high impedance material

In this case a purely geometrical interpretation of sound reflection cannot explain the echo structure, but the backscattering from the steel pipe can be predicted thanks to a generalization of the geometrical theory of diffraction (GTD).^{25,26} Apart from the specular echo the return is mainly composed, at the frequencies of interest, by the asymmetrical A_0 and symmetrical S_0 Lamb waves. These are plate waves traveling around the wall of the cylinder and expressions for their phase velocities are given in Ref. 27. The group velocities can be derived directly from these expressions.²⁸ Figure 2 plots the phase and group velocities matched to the thickness of the steel pipe.

According to the GTD, these plate waves are excited in the cylindrical shell close to the critical angle θ_c , which refers to the relation

$$\theta_c = \arcsin \left(\frac{c}{c_{\text{plate}}} \right), \quad (4)$$

where c_{plate} is the Lamb wave group velocity.

So the time delays between the specular echo and the Lamb waves can be evaluated by

$$\tau = 2a \left(\frac{1 - \cos \theta_c}{c} + \frac{\pi - \theta_c}{c_{\text{plate}}} \right). \quad (5)$$

The first term corresponds to the time difference between the specular reflection and the wavefront reaching the shell cyl-

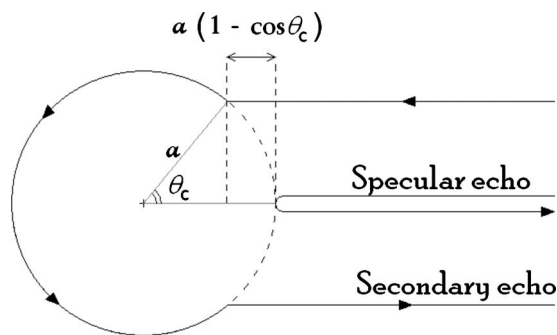


FIG. 3. Echo formation for shell cylinder following the GTD. Display of the geometrical path taken by the specular echo and the secondary echo.

inder at the critical angle. The second term gives the time for the plate wave to go once around the cylinder and be diffracted again at $-\theta_c$ (cf. Fig. 3). Because of the range of frequencies we are working with (the majority of energy is condensed in the band 50–100 kHz), the group velocity of the Lamb wave is stable (less than 8% variation for both Lamb waves, cf. Fig. 2). This means that the propagation is relatively non-dispersive, and the chirp rate and chirp duration for the secondary echoes are well preserved.

III. NUMERICAL SIMULATION

For more complex targets the theoretical analysis becomes intractable. In this section we demonstrate a numerical approach using a FDTD simulator, which provides a full wave equation solution as an alternative to analytic computation. The numerical model can also give new insights into the processes of echo formation to inform the development of new analytic solutions. Supported by simulations using FDTD, we propose a new model for the cylindrical shell with low impedance material based on an analogy with optical geometry.

A. Numerical approach: FDTD simulator

The FDTD method solves the elastic wave equation by discretization of the time-space domain.²⁹ This method takes into account the shear velocity within a solid object and so is able to model target resonances.³⁰ For an idealized infinite cylindrical shell, simulations can be run in two dimensions. Visualized as a circular cross section, these provide a good approximation to the behavior of the finite cylinder at broadside incidence.

Figure 4 provides a snapshot of the backpropagation of the simulated acoustic wave 1.1 ms after its interaction with the PVC tube, which is situated to the right of the image. The transmit signal is a linear chirp traversing 80–130 kHz over

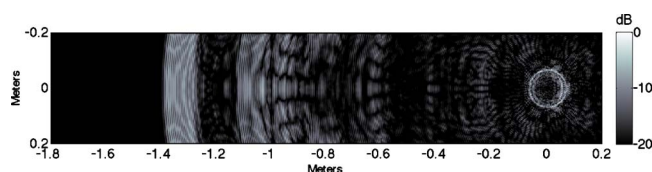


FIG. 4. (Color online) FDTD simulation showing the normalized sound pressure (in dB) for the echo of a PVC tube insonified with a linear chirp.

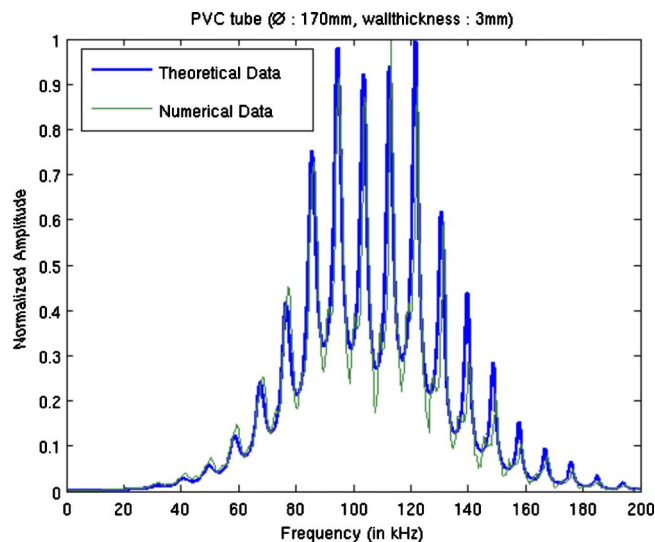


FIG. 5. (Color online) Matching between the analytical and numerical power spectra of the pressure field computed at the center of the PVC cylindrical shell.

0.06 ms. The simulated echo, traveling right to left, has the following structure in time: first, there is a large reflection from the front of the tube, followed at a distance corresponding to approximately twice the diameter by a reflection from the rear wall. Then we see a dense tail related to strong resonances inside the tube.

The influence of the inner resonances on the power spectrum is illustrated in Fig. 5. This shows the power spectrum calculated at the center of the modeled cylindrical shell for the numerical and theoretical approaches. The numerical spectrum is calculated using a 0.7 ms integration time from first arrival of the pulse. The theoretical spectrum has been adjusted according to spectral content of the transmit pulse. There is a high degree of concordance between the two with excellent agreement and collocation of peaks and troughs over the entire frequency range. This close agreement with the theoretical results for simple forms gives good confidence for the future value of numerical methods in estimating echoes from more complex targets.

B. Analogy with geometrical optics

For the PVC tube target, the simulator can also confirm that the first two main echo components are formed predominantly by reflections from the front and back of the cylinder. Figure 6 shows the interaction between the acoustic wave and the PVC tube and the formation of the echo structure. The incoming wave is seen passing beyond the cylinder to the right. The formation of the main echo fronts can be seen. The first, having reflected from the front face, is just approaching the left side of the image. The second is still forming within the pipe. The two echoes are cylindrical waves and the centers of these waves can be computed. The center of the first echo is situated at ~ 50 mm to the left of the cylinder center. The source of the second echo is ~ 45 mm to the right of the cylinder center.

These observations can be understood using a spherical mirror analogy from geometrical optics. In the case of reflec-

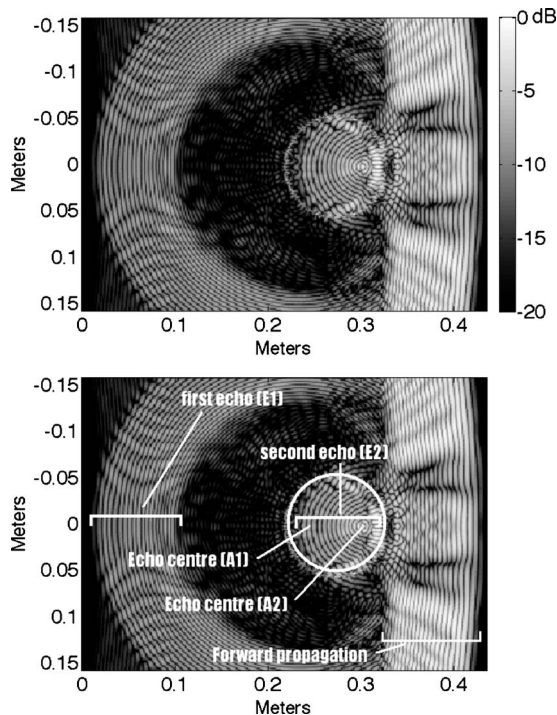


FIG. 6. Display of the normalized sound pressure expressed in dB. Visualization of the interaction between the incoming acoustic wave and the PVC shelled cylinder and the echo formation inside the target. In the lower annotated diagram the position of the cylinder is indicated by the bold circle.

tion at a spherical mirror the source image can be found using the formula given in Eq. (6). The notation is explained in Fig. 7 with reference to a concave mirror. C represents the center of the sphere, A is the source, and A' is the source image. Note that the formula is also valid for a convex mirror.

$$\frac{1}{SA'} + \frac{1}{SA} = \frac{2}{SC}. \quad (6)$$

The argument readily generalizes to the current case of a section through a cylinder with the images denoting line sources perpendicular to the plane of the page. We denote A_1 as the center of the first echo, corresponding to the reflection with a convex mirror of 170 mm diameter, and A_2 as the center of the second echo corresponding to the reflection with a concave mirror of 164 mm diameter. The dimensions of the mirrors correspond to the dimensions of the cylinder.

The values for CA_1 and CA_2 obtained using the acoustic response were given previously and were -50 and $+45$ mm, respectively. Using the optical equation Eq. (6) the source

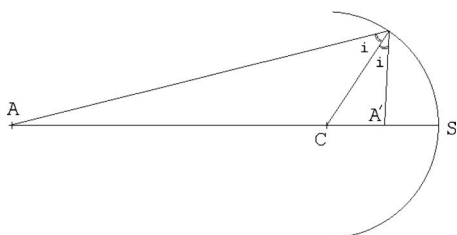


FIG. 7. Reflection by a concave spherical mirror, construction of the source image A' from the source A in the axis CS .

image locations $\overline{CA_1}$ and $\overline{CA_2}$ are -47 and $+42$ mm, respectively. The agreement between the results reinforces the assumption that the two first echoes are primarily due to reflections from the front and the back of the PVC tube.

IV. EXPERIMENTAL METHOD

The experimental program has been conducted using the biomimetic DBS developed jointly by the SPAWAR Systems Center, San Diego (SSC-SD) and the Applied Research Laboratory at the University of Texas (ARL-UT). The DBS has been designed to mimic both auditory and sound generation systems of the bottlenose dolphin with similar frequency bandwidths and sonar beamwidths.³¹ The projector and paired laterally positioned receivers are constructed from 1–3 piezocomposite transducer material. The DBS sensitivity gives a -3 dB bandwidth of approximately 60–130 kHz, and it is capable of delivering a series of arbitrary waveforms within this range. The transducers are mounted on a pan-and-tilt unit, allowing a mechanical scan of the area.

A. Signal design

A click taxonomy for dolphins has identified several click types based on distributions in two main spectral regions, one at low frequency (<70 kHz) and the other at higher frequency (>70 kHz).³² In an earlier paper we reported on a model for construction of biomimetic dolphinlike pulses from double down-chirp components, overlapping in both the time and frequency domains.³³ An interesting parallel can be drawn with pulses used by the echolocating big brown bat (*Eptesicus fuscus*). Similar time-frequency analyses have indicated that these signals are made up of three or four distinct downchirp components.^{34,35}

Demands on transducer and processing hardware are mitigated to some degree by making the pulses around 50% longer than natural dolphin signals, with a time duration of $120 \mu s$. The pulses cover a similar bandwidth to natural dolphin clicks (30–130 kHz) and the two downchirp components, each bounded by a Gaussian time window of $6\sigma = 100 \mu s$, are separated by $20 \mu s$. Following from analyses of clicks emitted by real dolphins performing target detection and localization tasks, the higher frequency chirp is always delayed relative to the lower frequency one. The only difference between the pulses is the bandwidth covered by the individual chirp components. Note that the given -3 dB bandwidth of the DBS indicates reduced energy in the low frequency band (30–60 kHz) compared to dolphins' sonar.

In total six biomimetic pulses have been designed and named DCn , where n varies from 1 to 6. All the pulses are based on the same model described earlier, and they only vary in the chirp rate (increasing linearly from DC1 to DC6). For the current work we have selected two of these pulses for comparison: DC1 and DC6. Their parameters are given in Table II.

The time signals and power spectra for DC1 and DC6 are displayed in Fig. 8. Note that for signal DC1 the two chirps have relatively high rates and are significantly overlapping. This pulse would be classified unimodal high frequency (type D) in the Houser taxonomy.³² In DC6 the two

TABLE II. Signal characteristics.

Signal	Chirp rate a (kHz s ⁻¹)	Nominal frequency bands	
		Chirp 1 (kHz)	Chirp 2 (kHz)
DC1	-0.420×10^6	30–114	46–130
DC6	-0.240×10^6	30–78	82–130

chirp components are well separated and the frequency distribution is clearly bimodal, designated as type C.

B. Tank experiments

Several tank experiments have been performed using the DBS with the synthetic dolphinlike pulses described above. These tests used the wave tank at Heriot–Watt University, which measures $12 \times 10 \times 4$ m³ deep and is concrete lined.

We are especially interested in the detailed spectral echo structures elicited using wideband pulses for discrimination purposes. The targets of interest here are the open-ended cylinders used for building the analytic and numerical models in Secs. II and III. As previously noted, these objects have similar target strengths (e.g., 1.6 dB difference at 100 kHz) and

similar dimensions (only 2 mm difference between the outer diameters, cf. Table I), making them very difficult to distinguish in intensity only data. However, they are made of different materials (steel and PVC) and, according to the models, are expected to have sufficiently different wideband echo structures for discrimination purposes.

The targets' responses were measured under identical conditions situated 8.90 m from the head of the DBS on the bottom of the test tank. In addition to the cylinder echoes the received signals contain significant reverberation returns from the surface water-air interface and from the tank floor.

1. Time-frequency observations and echo timings

Time-frequency representations offer a richer description for understanding echo phenomena than either time or frequency measures alone. Figure 9 displays spectrograms of the echoes from both tubes with signals DC1 and DC6. The spectrograms are computed with a Gaussian sliding window ($6\sigma = 100$ μ s). The unimodal and bimodal characteristics of the transmit pulses can be seen in the horizontal banding in the reverberation returns.

Comparing the PVC tube returns for both transmit signals, similar gross echo structures are seen. A first main echo

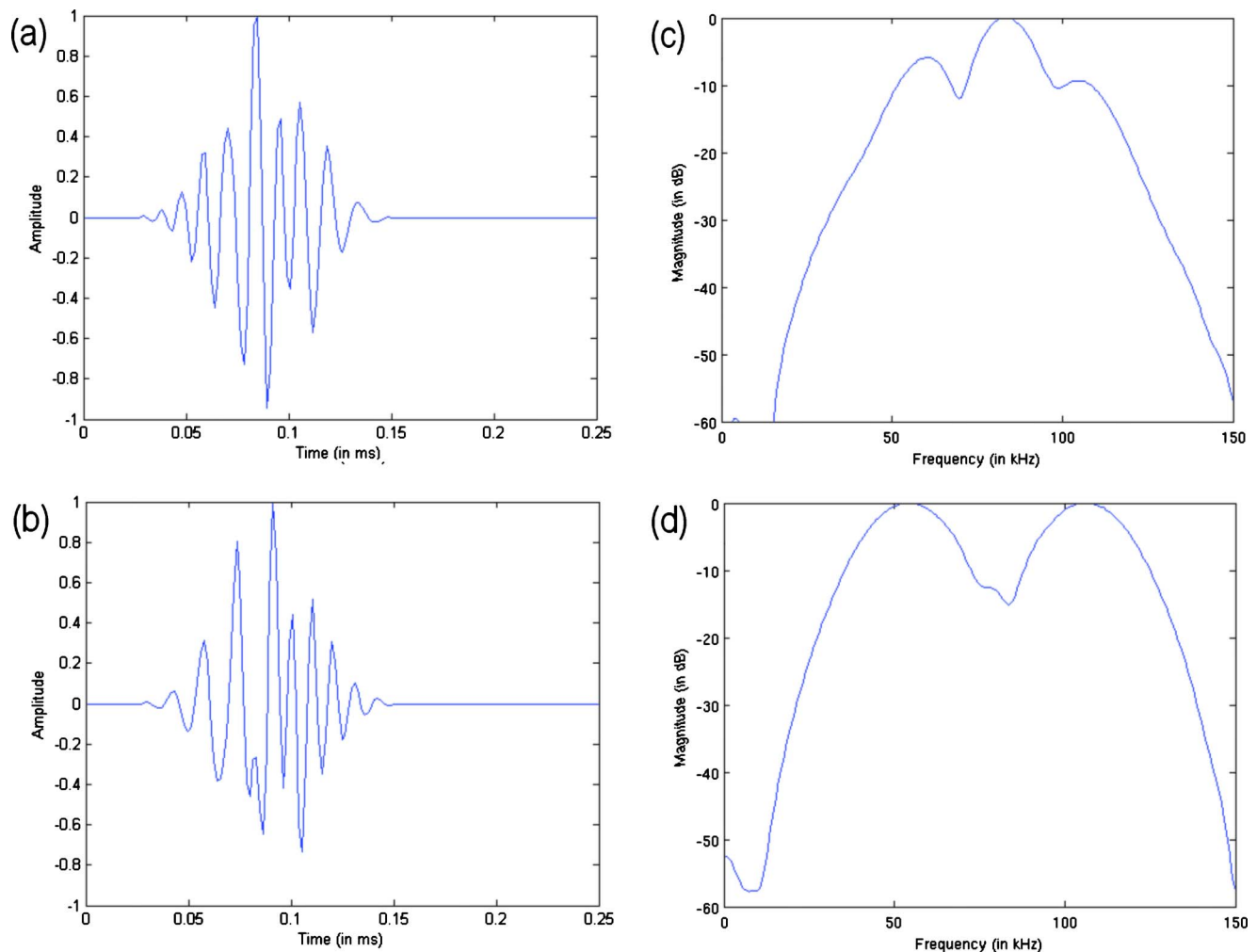


FIG. 8. (Color online) Display of two of the biomimetic pulses DC1 and DC6: (a) time signal of the DC1 pulse; (b) power spectrum of the DC1 pulse; (c) time signal of the DC6 pulse; and (d) power spectrum of the DC6 pulse.

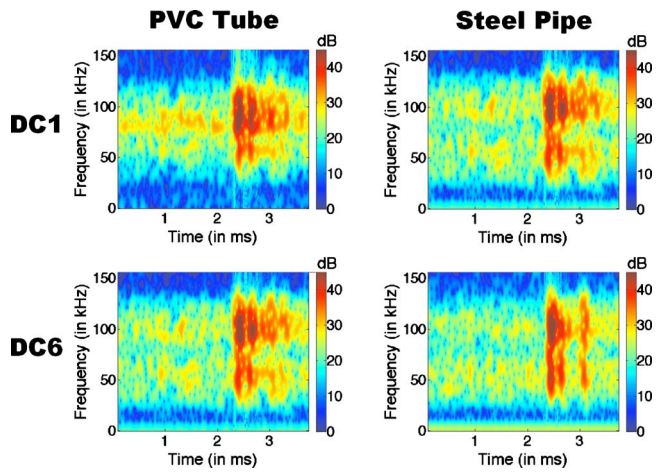


FIG. 9. (Color online) Spectrograms of PVC tube and steel pipe target echoes computed with a $100 \mu\text{s}$ sliding Gaussian window for pulses DC1 and DC6.

front (specular echo) is followed by a second large reflection. In this case the second echo corresponds to the reflection of the sound wave from the back of the cylinder. The second strong echo is followed by a “noisy” tail decreasing in amplitude over some 0.8 ms. Note that a similar pattern has been observed in the simulated echo in Sec. III A. This general structure is characteristic over all of the transmit signals used during experimentation.

Values for the inter-arrival times for the first two echo fronts in each case have been evaluated theoretically (cf. Eq. (3)) and by empirical measurement as $221.2 \mu\text{s}$ and $220.8 \mu\text{s}$. These have been estimated from peaks in the matched filter returns for signal DC1, which has better pulse compression properties than DC6. In both cases the diameter of the PVC tube is estimated with a precision better than 1 mm ($<1\%$ error).

For the steel pipe target, time delays relative to the S_0 wave have been computed theoretically (cf. Eq. (5)) and empirically as $100.6 \mu\text{s}$ and $103.1 \mu\text{s}$. For the A_0 wave the results are $153.3 \mu\text{s}$ and $152.4 \mu\text{s}$. The theoretical time delays have been computed at 100 kHz. Once again the empirical time delays have been estimated from peaks in the matched filter returns for signal DC1.

2. Spectral matching

Time-frequency representation is highly sensitive to the choice of windowing function and the selection made to provide sufficient resolution in echo timings above, loses oscillatory behavior in the spectrum. To regain this, the spectra must be calculated with a long enough window to integrate all of the key target echoes. Figure 10 shows the power spectral matching between the recorded echoes and the theoretical computations using a 0.6 ms Gaussian window (long enough to include the main target echoes). The theoretical curves have been adjusted for the DBS transmitter and receiver sensitivities.

Despite the noted differences in scattering physics for the two targets, the responses match well with theoretical predictions. Both targets provide evidence of oscillatory behavior through the ka band from 10 to 50, indicating good

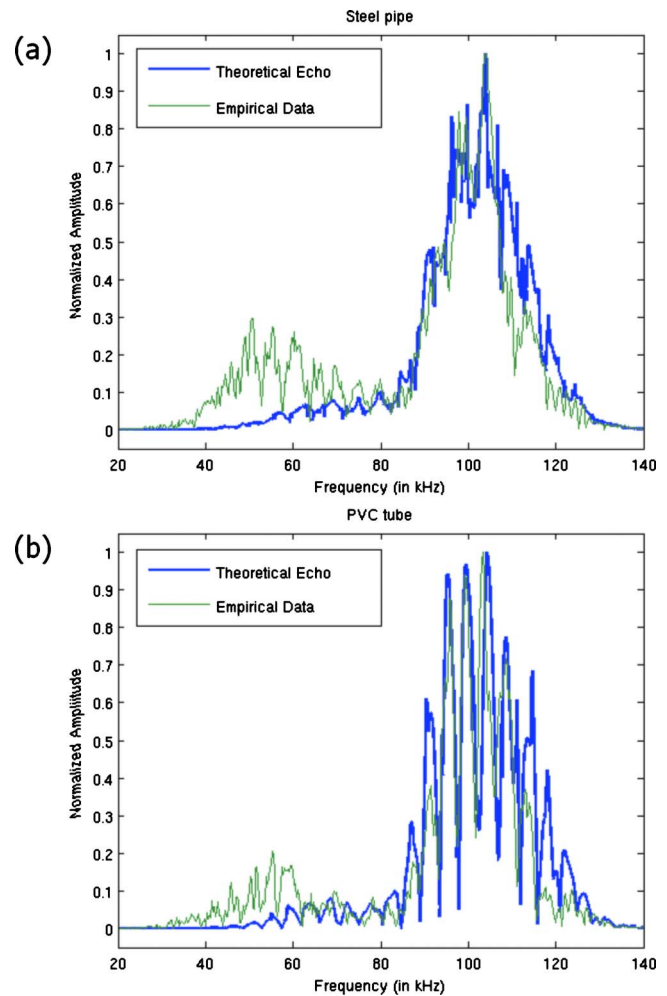


FIG. 10. (Color online) Matching between the theoretical and empirical DBS echoes power spectra for (a) steel pipe and (b) PVC tube. The high empirical response below 80 kHz due mainly to reverberation from the tank floor.

discrimination potential from the wideband DBS responses. An indication of how well the curves match is given by collocation of the extrema, both maxima and minima, for each of the curves. Looking first at the PVC tube response, between 80 and 130 kHz the maximum discrepancy in position for the peaks and troughs between the theoretical and empirical curves is approximately 1 kHz. The mean error is less than 0.1 kHz with variance of ≈ 0.5 kHz.

The heavily peaked form function for the PVC cylinder allows us to estimate parameters from the backscatter response curve in Fig. 10(b). The spectral notches are the strongest features and are the easiest to localize. An important consideration for discrimination of like targets is to relate the accuracy with which peak and notch positions can be determined to tolerances on physical parameters which influence the form function f_∞ . Processing the DBS returns with a time window ≥ 1 ms duration, we can readily measure spectral features with a precision of around 1 kHz. It is then possible to compute for tolerances on various physical parameters, which will keep the key resonance features within ± 1 kHz of the theoretical predictions for the exemplar target. The results are reported in Table III.

These values give an indication of the accuracy that can

TABLE III. Tolerances permitted in physical parameters of the PVC tube in order to keep the positions of resonance peaks and notches within ± 1 kHz band.

Cylinder parameters	Tolerance
Outer diameter	< 1 mm
Inner diameter	< 1 mm
ρ	$\pm 10\%$
c_l	$\pm 4\%$
c_t	$\pm 2\%$

be achieved in parameter estimation given certain prior assumptions, such as possible target shape, size, and material properties. Under the assumption of a cylindrical target, we can begin to extract size information from the wideband spectral response by relating the notch spacing Δf in the form function $|f_\infty|$ to the time spacing Δt between the two main echoes through the relation $\Delta f \Delta t = 1$.³⁶ In the case of the PVC tube we find a value of $\Delta f = 4.5$ kHz. The corresponding time spacing Δt_{PVC} is $222 \mu\text{s}$, equating to a cylinder diameter (cf. Eq. (3)) of 166 mm. These results are in line with expectations from the timing information given in Sec. IV B 1.

Note that the oscillations for the steel pipe are expected to be deeper over the bandwidth of 40–80 kHz, facilitating feature extraction and improving accuracy.

C. Noisy environment: Small cylinder responses in a harbor setting

The harbor experiments were carried out at Port Edgar, a working harbor and marina on the Forth Estuary near Edinburgh. This is a tidal site with a cluttered muddy seabed and shallow water, varying between 2 and 8 m in depth. In these experiments, the target under consideration is a one liter capacity aluminum bottle filled with seawater. The relevant target parameters concerning the aluminum bottle can be found in Table. I. The DBS was secured to a pontoon facing the target at 20 m range. The platform supporting the DBS was stable enough to ignore any Doppler effect. Even considering a 1 m s^{-1} velocity of the sonar relative to the target, and the smallest wavelength supported by the DBS (1.25 cm at 120 kHz), the maximum shift in frequency will be 80 Hz, which is far below the 1 kHz precision of the sensor. In this sense, Doppler effects will not adversely affect the localization of notches in the echo spectra of the target. Both sonar and target were 1 m below the surface, and the depth of the water at the time of the experiment was 3 m. In addition to the shallow water setting, acoustic target detection and identification are made more difficult by the movement of boats, dredging and piling activity in the estuary, and with the influence of waves and prevailing weather conditions. The figures in Table III show that even small changes in target parameters will modify the locations of the features we wish to use for classification. The current section demonstrates that it is still possible to extract these features even for a small target in a noisy shallow water environment and at ranges not achievable in the test tank.

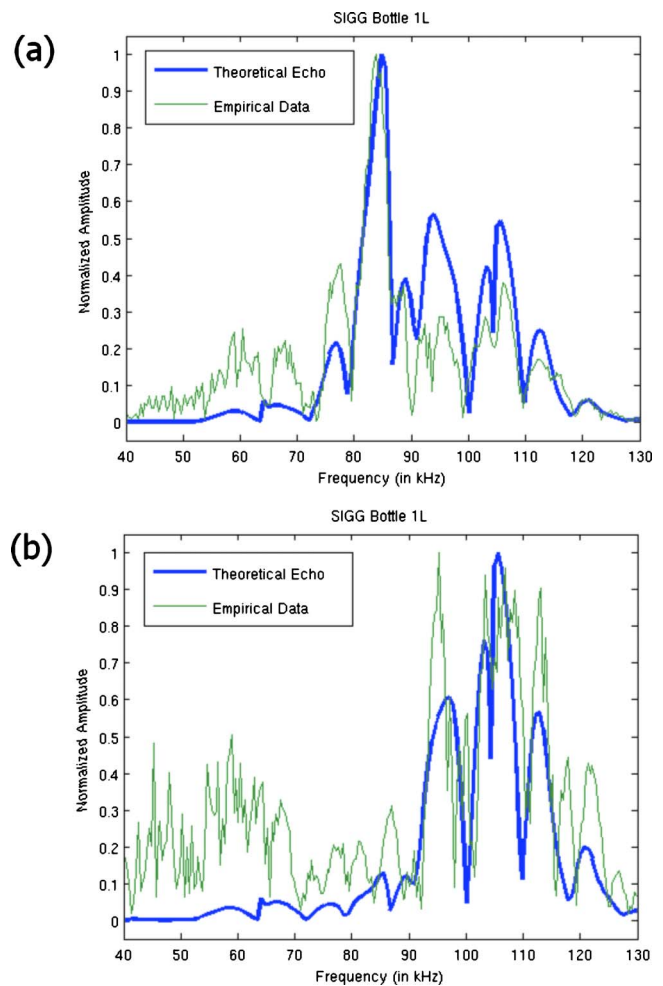


FIG. 11. (Color online) Matching between the theoretical and empirical DBS echoes power spectra for the aluminum bottle with (a) DC1 pulse and (b) DC6 pulse. The empirical spectrum has been computed using a single echo of the bottle.

Following our previous methodology, we model the aluminum bottle using a simplified, infinite cylindrical shell approximation. Given the short length of the cylinder (200 mm), artifacts from the bottle end caps and the low signal-to-noise ratio (SNR), we cannot expect to achieve the same degree of correspondence between theoretical and empirical data as in the tank tests. However, the comparison between the model predictions and the measured response (Fig. 11) does show good agreement in principal peak and notch positions. For this target/environment combination, pulse DC1 gives consistently better results than DC6. A discussion of the influence of noise and required SNR for classification follows in Sec. V A.

V. CLASSIFICATION

The models and empirical data presented above show that echoes from targets producing multiple returns are characterized by interferences in the spectra. For certain targets we can relate features of the spectra, particularly notch locations and spacings, to specific physical properties. In this section we propose a new metric for the classification of broadband echoes based on the localization of the interference notches.

TABLE IV. (Top) Confusion matrix relative to the DC1 pulse echoes and (bottom) confusion matrix relative to the DC6 pulse echoes. These matrices have been computed with 40 measurements per target.

DC1		Cone	Cone 8° tilted	Pipe	Tube	Rocket head	Brick (length)	Brick (width)
Classifier decision	Cone	0.50	0.26	0	0.06	0	0	0
	Cone 8° tilted	0.32	0.56	0.47	0.16	0	0	0
	Pipe	0.12	0.06	0.43	0	0	0	0
	Tube	0.06	0.03	0.05	0.78	0	0	0
	Rocket head	0	0.09	0	0	1.00	0.21	0
	Brick (long)	0	0	0.05	0	0	0.79	0
	Brick (large)	0	0	0	0	0	0	1.00
DC6		Cone	Cone 8° tilted	Pipe	Tube	Rocket head	Brick (length)	Brick (width)
Classifier decision	Cone	0.44	0.44	0	0	0	0	0
	Cone 8° tilted	0.35	0.44	0.05	0	0	0	0
	Pipe	0.12	0	0.81	0.06	0	0	0
	Tube	0.09	0.12	0	0.94	0	0	0
	Rocket head	0	0	0.14	0	1.00	0	0
	Brick (long)	0	0	0	0	0	1.00	0
	Brick (large)	0	0	0	0	0	0	1.00

Let F be the spectrum of the broadband echo. Let $\{\omega_i\}_{i \in [1, N]}$ be the location in frequency of the notches of F . To F we associate ΔF such that

$$\Delta F(\omega) = \sum_{i=1}^N \delta(\omega - \omega_i) * G_{\sigma}(\omega), \quad (7)$$

where δ represents the Dirac function and G_{σ} is the centered Gauss function with a variance of σ . Given the capability of the sonar, we choose the value of parameter σ to match the 1 kHz precision we wish to achieve in notch location. The associated function ΔF is an irregular Gaussian comb where the peaks represent the notch locations.

In this space we define the Euclidian distance between two elements ΔF and ΔG as

$$d(\Delta F, \Delta G) = \left(\int_0^{+\infty} |\Delta F(\omega) - \Delta G(\omega)|^2 d\omega \right)^{1/2}. \quad (8)$$

Classification using the distance metric has been tested using the PVC (tube) and steel (pipe) cylinders along with three other targets: an 800 mm long aluminum conical shell (cone) with diameter reducing from 500 to 20 mm along its length, a solid aluminum nose cone (rocket head) $200 \times 120 \text{ mm}^2$ (height \times diameter), and a non-resonant concrete brick measuring $200 \times 100 \times 50 \text{ mm}^3$. The cone and the brick have been insonified with two different orientations: vertical and tilted 8° for the cone, and lengthways and widthways for the brick. As before the targets were placed on the tank floor approximately 8.90 m from the center of the DBS array. Although the tank floor is relatively flat compared to the minimum wavelength, the reverberation introduces coherent noise in the data. Each target has been insonified 21 times with head angle varying from -10° to $+10^\circ$ in 2° intervals.

The echo corresponding to the target is extracted from each record, and the power spectrum is computed. The notches corresponding to local minima within a 2 kHz wide sliding window are extracted in the 60–130 kHz band, which

corresponds to the most significant frequencies of the DBS. The 2 kHz sliding window just ensures that the notches do not overlap in the computation of the ΔF function. From the location of the notches, the ΔF function is computed using Eq. (7) for each echo spectrum. In order to classify the targets one reference ΔF_{ref} is needed for each target. For the cone, tilted cone, rocket head, brick (length), and brick (width) target a single broadside echo has been recorded as the reference. The reference functions ΔF_{ref} for the PVC tube and steel pipe are computed from synthetic echoes. Thanks to the models proposed in Sec. II C, the timing between the specular echo and the secondary echoes can be estimated with excellent precision. Synthetic echoes for these targets are built simply using the timing and the relative phase shift between the primary and the secondary echoes. Thus, the PVC tube and steel pipe ΔF_{ref} functions come solely from the notch locations given by analytical models.

The classifier uses a simple nearest neighbor algorithm. Table IV displays confusion matrices for the two signals DC1 and DC6. In both cases the matrices demonstrate that this simple metric provides a good discriminant, but the two pulses do show different results. The pulses focus energy on different frequency bands, and in this experiment, DC6 proves more effective in classifying the full set of targets, but DC1 shows better results in discriminating the cone orientation. Note that there is no misclassification between the resonant shelled targets and the solid concrete brick using DC6, and very little between solid and hollow target using either pulse. We can conclude that information related to the target structure is linked to the inner resonances of the target and that we can gain access to this information through the interference notches. Using several pulses with different frequency bands allows us to focus the classifier on relevant spectral regions for a particular target.

Another point of interest arises from the confusion matrices: the confusion between the two cone aspects is high (between 30% and 45%), because it is fundamentally the

TABLE V. Confusion matrix for the fusion system of the two classifiers relative to the two pulses.

DC1 and DC6		Cone				Rocket	Brick	Brick
		Cone	8° tilted	Pipe	Tube	head	(length)	(width)
Classifier decision	Cone	0.50	0.21	0	0	0	0	0
	Cone 8° tilted	0.29	0.59	0.05	0	0	0	0
	Pipe	0.12	0	0.81	0.06	0	0	0
	Tube	0.09	0.12	0	0.94	0	0	0
	Rocket head	0	0.08	0.14	0	1.00	0	0
	Brick (long)	0	0	0	0	0	1.00	0
	Brick (large)	0	0	0	0	0	0	1.00

same target and the change in look angle is small (8°), so the resonances are expected to be similar. Note that the cone is classified correctly (independently of orientation) at 82.3% and 83.8% for DC1 and DC6, respectively. For the brick, the change in orientation is 90° , the scattering points are in a totally different configuration and the locations of the notches are significantly shifted. So there is no confusion between these two configurations.

The results can be optimized with fusion algorithms. In our case we use the Dempster–Shafer theory of evidence,³⁷ with confusion matrices for DC1 and DC6, giving an approximation of the belief functions. The final fusion decision is based on the rule of maximum belief. We run two classifiers, corresponding to pulses DC1 and DC6, for each view of a target. The belief functions are generated from the results of each classifier, given its expected performance estimated from the confusion matrix (the probability of correct classification). Over both belief functions, the maximum belief is chosen. Table V gives the confusion matrix fusing the results from both pulses. The fused result is better than either classifier independently. While DC1 performs better in classifying the cone, and distinguishing its two aspects, DC6 is better classifying the pipe and tube. The fused classifier takes advantage of the best results of each classifier for each individual target.

A. Influence of the noise

In Secs. II and III, we explained formation of characteristic spectral patterns from interferences between primary

and secondary target echoes. The null estimator exploits these interferences for discrimination. Since both primary and secondary echoes are required, the strength of the secondaries is crucial in determining performance of the classifier in noise. Defining SNR as the ratio of the peak of the secondary echoes to the noise level, Fig. 12 displays the ΔF function for the PVC tube insonified by pulse DC1 against increasing levels of additive Gaussian white noise. With SNR above 15 dB, the notches are well localized across the band. From 15 to -5 dB, the influence of the noise is apparent, but the frequency band of 80–110 kHz, corresponding to the highest sensitivity of the DBS, remains stable and can be used for classification. At still lower SNR, with noise levels in excess of the peak secondary echoes, the target resonances are masked and the classifier will fail.

VI. CONCLUSIONS

Working from acoustics theory, numerical models, and empirical data, we have shown that the resonances of a shelled object insonified at broadside are stable and consistent, giving rise to characteristic patterns of notches in the echo spectrum. We have identified a spectral range of ka , from 10 to 40, as providing good spectral information for target discrimination, and note that this corresponds well with the frequency capability of natural dolphin sonar and the biomimetic DBS system for a variety of targets of interest in military, offshore, and scientific survey applications. The notch spacings are related directly to timings of multiple echoes from the target and can, in turn, be related to physical scattering and diffraction models so that target dimensions and material properties can be estimated, assuming the sensor characteristics are taken into account. In this paper we have shown that the notch locations provide excellent features for target classification and have introduced an effective distance metric based on these features.

ACKNOWLEDGMENTS

Thanks are due to the Office of Naval Research for support under the NICOP program (Grant No. N00014-05-1-0725), and to the Scottish Funding Council for supporting the Joint Research Institute in Signal and Image Processing between the University of Edinburgh and Heriot–Watt University, part of the Edinburgh Research Partnership in Engineering and Mathematics (ERPEM).

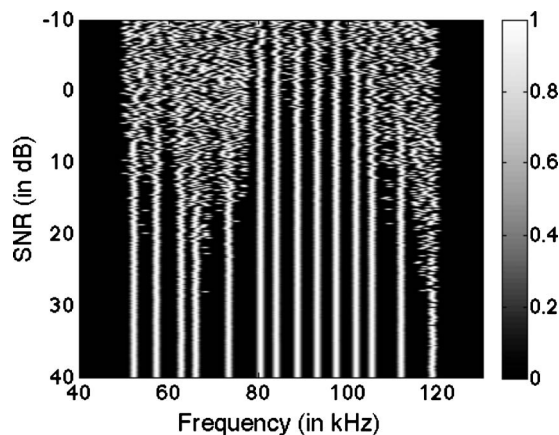


FIG. 12. ΔF function of the echo of PVC tube with an increasing synthetic white noise.

APPENDIX: COMPUTATION OF F_∞

Given the form function f_∞ represented by $\sum_{n=0}^{\infty} (-1)^n \epsilon_n b_n$, we show that f_∞ is well approximated by a truncation of the infinite sum so that $f_\infty(ka) \approx \sum_{n=0}^N (-1)^n \epsilon_n b_n$ with $ka < N/2$.

We begin by analyzing the b_n term given by Eq. (A1). The expression of each term in the determinants in Eq. (A1) can be found in Ref. 18.

$$b_n = \begin{vmatrix} b_{11} & a_{12} & a_{13} & a_{14} & a_{15} & 0 \\ b_{21} & a_{22} & a_{23} & a_{24} & a_{25} & 0 \\ 0 & a_{32} & a_{33} & a_{34} & a_{35} & 0 \\ 0 & a_{42} & a_{43} & a_{44} & a_{45} & a_{46} \\ 0 & a_{52} & a_{53} & a_{54} & a_{55} & a_{56} \\ 0 & a_{62} & a_{63} & a_{64} & a_{65} & 0 \\ \hline a_{11} & a_{12} & a_{13} & a_{14} & a_{15} & 0 \\ a_{21} & a_{22} & a_{23} & a_{24} & a_{25} & 0 \\ 0 & a_{32} & a_{33} & a_{34} & a_{35} & 0 \\ 0 & a_{42} & a_{43} & a_{44} & a_{45} & a_{46} \\ 0 & a_{52} & a_{53} & a_{54} & a_{55} & a_{56} \\ 0 & a_{62} & a_{63} & a_{64} & a_{65} & 0 \end{vmatrix}. \quad (\text{A1})$$

Let $\det(D) = \det(d_{ij})$, the numerator in Eq. (A1). Using a determinant expansion by minor following the columns, we can write

$$\det(D) = \sum_{\sigma \in \Omega} (-1)^{i(\sigma)} \prod_{j=1}^6 d_{\sigma(j)j}, \quad (\text{A2})$$

where Ω is the set of all the permutations of $[1,6]$ and $i(\sigma)$ is the number of permutation inversions in permutation σ . So

$$|\det(D)| \leq 6! \max_{\sigma \in \Omega} \left| \prod_{j=1}^6 d_{\sigma(j)j} \right|. \quad (\text{A3})$$

The behavior of each column is dominated by a specific Bessel function: the Bessel function of the first kind J_n for columns 1, 2, 4, and 6, and the Bessel function of the second kind N_n for columns 3 and 5. So we would expect the behavior of $|\prod_{j=1}^6 d_{\sigma(j)j}|$ to follow the form $J_n^4 N_n^2$.

Given

$$\begin{aligned} J_n(z) &= \frac{1}{2\pi j} \oint e^{(z/2)(t-(1/t))} t^{-n-1} dt \\ &= \frac{1}{2\pi} \int_0^{2\pi} e^{(z/2)(\alpha-(1/\alpha))(\cos \omega + j \sin \omega)} \frac{e^{-jn\omega}}{\alpha^n} d\omega \end{aligned}$$

with $\alpha > 0$, we can write

$$\begin{aligned} |J_n| &\leq \frac{1}{2\pi} \int_0^{2\pi} \frac{e^{(z \cos \omega/2)(\alpha-(1/\alpha))}}{\alpha^n} d\omega \\ &\leq \frac{1}{2\pi} \int_0^{2\pi} \frac{e^{(z\alpha \cos \omega/2)}}{\alpha^n} d\omega \leq \frac{e^{(\alpha z/2)}}{\alpha^n} = f(\alpha). \end{aligned}$$

We next choose α in order to minimize $f(\alpha)$

$$\frac{df}{d\alpha} = 0 \Leftrightarrow \alpha = \frac{2n}{z}$$

and arrive at the majoration

$$|J_n(z)| \leq \left(\frac{ze}{2n} \right)^n. \quad (\text{A4})$$

We can see that for $z \leq n/2$, $|J_n| \rightarrow 0$.

The Bessel function of the second kind can be written as follows:³⁸

$$N_n = AJ_n + BJ_n \int \frac{dx}{xJ_n^2},$$

where A and B are constants, so that

$$N_n J_n = AJ_n^2 + BJ_n^2 \int \frac{dx}{xJ_n^2}.$$

It can be shown through a series approximation that $J_n^2 \int (dx/xJ_n^2) = O(1)$ for $z < n/2$. This implies that the product $J_n^4 N_n^2$ can be bounded by $A(ze/2n)^{2n}$, with A as constant.

Turning to the denominator in Eq. (A1), using the same determinant expansion over the columns, the behavior should follow the characteristic $(J_n N_n)^3$, which remains roughly constant for $z \leq n/2$. Thus, the b_n coefficient can be bounded by $A'(ze/2n)^{2n}$. We can verify that the function $\sum_{n=N}^{+\infty} (ze/2n)^{2n} \leq \sum_{n=N}^{+\infty} (Ne/4n)^{2n} = r(N)$ decreases very quickly to 0. For example, with $N=20$, we find $r(N) \approx 2 \times 10^{-7}$.

¹D. Boulinguez and A. Quinquis, "Classification of underwater objects using Fourier descriptors," in Proceedings of the International Conference on Image Processing and Application (Manchester, UK, July 1999).

²S. W. Perry and L. Guan, "Detection of small man-made objects in sector scan imagery using neural networks," *Proc. IEEE Int. Conf. on Oceanic Engineering*, Vol. 4, pp. 2108–2114, Honolulu, HI, 2001.

³E. Dura, J. Bell, and D. Lane, "Superellipse fitting for the recovery and classification of mine-like shapes in sidescan sonar images," *IEEE J. Ocean. Eng.* 33, 434–444 (2008).

⁴M. G. Bello and G. J. Dobeck, "The use of texture measures in improving mine classification performance," in Proceedings of the OCEANS 2003 (2003).

⁵I. Quidu, J. Malkasse, G. Burel, and P. Vilbe, "Mine classification using a hybrid set of descriptors," in Proceedings of the OCEANS 2000 MTS/IEEE Conference and Exhibition, Vol. 1, 291–297 (2000).

⁶S. Reed, Y. Petillot, and J. Bell, "An automatic approach to the detection and extraction of mine features in sidescan sonar," *IEEE J. Ocean. Eng.* 28, 90–105 (2003).

⁷G. J. Dobeck, "Algorithm fusion for automated sea mine detection and classification," in Proceedings of the Oceans '01 Conference, Vol. 1, 130–134 (2001).

⁸T. Aridgides, M. Fernandez, and G. Dobeck, "Processing string fusion for automated sea mine classification in shallow water," in Proceedings of the Oceans '02 MTS/IEEE, Vol. 4, 2168–2175 (2002).

⁹T. Aridgides and M. Fernandez, "Cascaded Volterra fusion of processing strings for automated sea mine classification in shallow water," in Proceedings of the OCEANS 2005 MTS/IEEE, Vol. 2, 1636–1643 (2005).

¹⁰P.-Y. Mignotte, E. Coiras, H. Rohou, Y. Petillot, J. Bell, and K. Lebart, "Adaptive fusion framework based on augmented reality training," *IEE Proc., Radar Sonar Navig.* 2, 146–154 (2008).

¹¹H. Lew, "Broadband active sonar: Implications and constraints," Technical Report No. DSTO-TR-0435, Melbourne, Australia (1996).

¹²D. B. Reeder, J. M. Jech, and T. K. Stanton, "Broadband acoustic backscatter and high resolution morphology of fish, Part 1: Measurements," in Proceedings of the ICES Symposium on Acoustics in Fisheries and Aquatic Ecology (Montpellier, France, June 2002).

¹³W. L. Michael, J. M. Jech, and D. A. Demer, "Multi-frequency echo-

- classification and target strength measurements of Atlantic herring," in Proceedings of the ICES Symposium on Acoustics in Fisheries and Aquatic Ecology (Montpellier, France, June 2002).
- ¹⁴T. K. Stanton, D. B. Reeder, and J. M. Jech, "Inference of fish orientation from broadband acoustic echoes," in Proceedings of the ICES Symposium on Acoustics in Fisheries and Aquatic Ecology (Montpellier, France, June 2002).
- ¹⁵W. Au, *The Sonar of Dolphins* (Springer-Verlag, Berlin, 1993).
- ¹⁶Y. Pailhas, C. Capus, and J. Bell, "Modelling for obstacle avoidance sonar design," Proceedings of the Institute of Acoustics (IOA) (2005).
- ¹⁷P. Nachtigall, "Odontocete echolocation performance on object size, shape, and material," in *Animal Sonar Systems*, R. G. Busnel and J. F. Fish, eds. (Plenum, New York, 1980), pp. 71–95.
- ¹⁸R. Doolittle and H. Uberall, "Sound scattering by elastic cylindrical shells," *J. Acoust. Soc. Am.* **39**, 272–275 (1966).
- ¹⁹R. Hickling, "Analysis of echoes from a solid elastic sphere in water," *J. Acoust. Soc. Am.* **34**, 1582–1592 (1962).
- ²⁰T. Stanton, "Sound scattering by cylinders of finite length. III. Deformed cylinders," *J. Acoust. Soc. Am.* **86**, 691–705 (1989).
- ²¹G. Kino, *Acoustic Waves* (Prentice-Hall Signal Processing Series, Englewood Cliffs, NJ, 1987).
- ²²G. Gaunaurd and H. Uberall, "RST analysis of monostatic and bistatic acoustic echoes from an elastic sphere," *J. Acoust. Soc. Am.* **73**, 1–12 (1983).
- ²³M. Hasan and M. Azimi-Sadjadi, "A modified block FTF adaptive algorithm with applications to underwater target detection," *IEEE Trans. Signal Process.* **73**, 1–12 (1996).
- ²⁴G. Gaunaurd and H. Strifors, "Frequency- and time-domain analysis of the transient resonance scattering resulting from the interaction of a sound pulse with submerged elastic shells," *IEEE Trans. Signal Process.* **40**, 313–324 (1993).
- ²⁵P. L. Marston, "GTD for backscattering from elastic spheres and cylinders in water, and coupling of surface elastic waves with the acoustic field," *J. Acoust. Soc. Am.* **83**, 25–37 (1988).
- ²⁶S. G. Kargl and P. L. Marston, "Observations and modeling of the backscattering of short tone bursts from spherical shell: Lamb wave echoes, glory, and axial reverberation," *J. Acoust. Soc. Am.* **85**, 1014–1028 (1989).
- ²⁷H. Lamb, "On waves in an elastic plate," *Proc. R. Soc. London Ser. A* **93**, 114–128 (1917).
- ²⁸T. N. Grigsby and E. J. Tajchman, "Properties of lamb waves relevant to the ultrasonic inspection of thin plates," *IEE Trans. Ultrason. Eng.* **8**, 26–33 (1961).
- ²⁹L. Collatz, *The Numerical Treatment of Differential Equations* (Springer-Verlag, Berlin, 1966).
- ³⁰J. M. Bell and M. Lianantonakis, "Analysis of target scattering using a finite difference time domain model," *IOA Conf. on Sonar Transducers and Numerical Modelling in Underwater Acoustics*, Vol. 27, Pt. 1, Teddington, UK (2005).
- ³¹D. Houser, S. Martin, M. Phillips, E. Bauer, T. Herrin, and P. Moore, "Signal processing applied to the dolphin-based sonar system," in Proceedings of the OCEANS 2003, Vol. 1, 297–303 (Oceans 2003 MTS/IEEE, San Diego, CA, September 2003).
- ³²D. Houser, D. Helweg, and P. Moore, "Classification of dolphin echolocation clicks by energy and frequency distributions," *J. Acoust. Soc. Am.* **16**, 1576–1585 (1999).
- ³³C. Capus, Y. Pailhas, K. Brown, D. Lane, P. Moore, and D. Houser, "Bio-inspired wideband sonar signals based on observations of the bottlenose dolphin (*Tursiops truncatus*)," *J. Acoust. Soc. Am.* **121**, 594–604 (2007).
- ³⁴A. Bultan, "A four-parameter atomic decomposition of chirplets," *IEEE Trans. Signal Process.* **47**, 731–745 (1999).
- ³⁵C. Capus and K. Brown, "Short-time fractional Fourier methods for the time-frequency representation of chirp signals," *J. Acoust. Soc. Am.* **113**, 3253–3263 (2003).
- ³⁶G. C. Gaunaurd, D. Brill, H. Huang, P. W. B. Moore, and H. C. Strifors, "Signal processing of the echo signatures returned by submerged shells insonified by dolphins "clicks": Active classification," *J. Acoust. Soc. Am.* **103**, 1547–1557 (1998).
- ³⁷G. Shafer, *A Mathematical Theory of Evidence* (Princeton University Press, Princeton, NJ, 1976).
- ³⁸M. Abramowitz and I. Stegun, *Handbook of Mathematical Functions* (Dover Publication, New York, 1965).